Role of localized electrons in electron-hole interaction: The case of $SrTiO_3$

Lorenzo Sponza, Valérie Véniard, Francesco Sottile, Christine Giorgetti, and Lucia Reining
Laboratoire des Solides Irradiés, Ecole Polytechnique, CNRS, CEA-DSM, F-91128 Palaiseau, France and European Theoretical Spectroscopy Facility (ETSF)

(Received 8 March 2013; revised manuscript received 26 April 2013; published 3 June 2013)

Strontium titanate $SrTiO_3$ is an extensively studied material. Of particular interest are its electronic properties. Here we present a theoretical study of its optical spectrum on the basis of state-of-the-art calculations including many-body effects. The latter are evaluated by solving the Bethe-Salpeter equation within the GW approximation for the self-energy. Excitonic effects are strong at the onset and at higher energies up to 10 eV. Agreement between theory and experiment is excellent at the onset, but only qualitative at higher energies, where excitonic effects are stronger in theory than in experiment. The origin of structures in the spectrum, as well as the remaining discrepancy between theory and experiment, are discussed. We also present benchmark results for calculations using more approximate ways to determine the spectra, including simplified time-dependent density-functional theory.

DOI: 10.1103/PhysRevB.87.235102 PACS number(s): 71.15.Qe, 71.20.−b, 71.35.−y, 78.20.Bh

I. INTRODUCTION

Strontium titanate $SrTiO_3$ (STO) (pure, doped, or in junctions) displays several peculiar properties which make this material widely investigated for technological applications and for a theoretical understanding of basic processes. It is prototypical among the transition-metal oxides and therefore has been often taken as a benchmark material to test the performances of different theories.[1–3] Of interest are its conducting,[4–6] structural,[7–9] and magnetic[10] properties. All these features are closely related to its electronic structure. Optical spectroscopy techniques (electron energy loss, reflectivity, ellipsometry, and absorption) are powerful tools to probe valence and conduction states, being in many cases the experiments of choice to get insight into the electronic properties. Optical spectra of STO measured in a different range of energy and with different techniques (reflectivity,[11–14] ellipsometry,[14,15] x-ray absorption spectroscopy,[16] and others) were compared early on with theoretical works, mostly calculations based on the independent-particle (IP) picture.[17,18] More recent *ab initio* calculations include all-electron[19–23] and plane-wave-pseudopotential approaches,[24] but to our knowledge, optical properties have always been calculated using Fermi's golden rule in the IP framework, where the spectrum is given by a simple sum over all possible transitions.

However, a real absorption experiment is more complex. Electrons excited from valence to empty conduction states induce a response in the whole electronic system polarizing the medium (screening) while the interaction between the excited electron and the hole modifies the spectral shape and can give rise to bound or continuum correlated electron-hole states (excitons). Moreover, the dynamically polarized medium can react in many ways, e.g., creating additional electron-hole pairs (multiple exciton generation[25]) or exciting vibrational degrees of freedom (electron-phonon coupling[26–28]). The simple IP picture is not sufficient to describe these processes, which are instead included in principle in a many-body approach.

The aim of the present work is to give a more realistic description and analysis of the optical properties of STO. We have concentrated in particular on features that are peculiar for this material; most importantly, we are interested in analyzing the interplay between empty d states and the occupied O $2p$ states. Localized d electrons must be treated carefully: at the optical level they can give rise to sharp peaks and strongly bound electron-hole pairs. We have computed the dielectric function of STO in the framework of many-body perturbation theory[29] (MBPT) on the level of the GW approximation,[30] solving the Bethe-Salpeter equation (BSE) in a fully *ab initio* framework.[31] The approach includes nonlocal self-energy effects and the electron-hole interaction (excitons), whereas lattice polarizability (electron-phonon coupling) as well as dynamical effects in the electron-hole interaction are neglected. Moreover, we have tested different approximations that allow one in principle to perform more efficient calculations, including simple kernels used in the framework of time-dependent density-functional theory (TDDFT).[32] Results are compared with experiments.[14,33] The remaining discrepancies between theory and experiments are discussed.

The paper is organized as follows: Sec. II contains background information concerning the material as well as the theoretical approaches that have been used. In Sec. III, results are presented and discussed; these include band structure, projected density of states, and spectra. Finally, Sec. IV presents the conclusion.

Atomic units are used ($e = \hbar = m_e = 1/4\pi\epsilon_0 = 1$), unless stated otherwise.

II. BACKGROUND

A. Geometry and crystal-field splitting

Strontium titanate (STO) is a transition-metal oxide, which crystallizes at room temperature in the cubic perovskite structure of the kind ABO_3, with a lattice parameter $a = 3.905$ Å.[34] Its fundamental absorption edge is around 3.2 eV at room temperature,[11,14] and the direct gap is 3.75 eV.[14]

In such materials, the A atoms (Sr) occupy the corners of a cubic lattice, the B atom (Ti) occupies the center of the cube, and O atoms lay at the center of the faces of the cubic cell, as shown in Fig. 1.

The presence of the oxygens around the A and B ions breaks the atomic spherical symmetry, removing the fivefold degeneracy of the d levels of A and B atoms (crystal-field effect). The atomic fivefold-degenerate d levels split into two

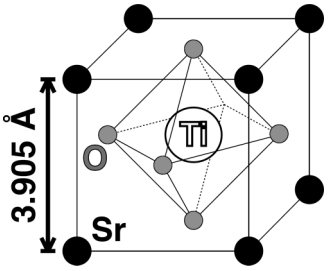

FIG. 1. Atomic position in the cubic STO cell. Ti (empty circle) lay on the center of the cell, O atoms (gray circles) form an octahedron centered on the Ti atom, and Sr atoms (black circles) sit at the corners of the cell.

subgroups according to their symmetry properties. The three orbitals labeled d_{xy}, d_{yz}, and d_{zx} form the t_{2g} group. The remaining two orbitals labeled d_{z^2} and $d_{x^2-y^2}$ form the e_g group. The respective energy position of e_g and t_{2g} depends on the symmetry of the environment of the cations.[35]

Since A ions are surrounded by 12 O, they are in a dodecahedral symmetry, so the three A t_{2g} orbitals are at higher energy than the two A e_g orbitals. The B ions are surrounded by six O ions, corresponding to an octahedral symmetry, with the consequence that the three t_{2g} orbitals are at lower energy than the two e_g orbitals (see Fig. 2). The energy of the different levels is in agreement with recent *ab initio* DFT calculation on electronic properties of $SrTiO_3$.[36] There is a slight difference to the experimental assignment from Ref. 14, where e_g and t_{2g} states of Sr are reversed, but since the states are significantly hybridized and our assignment refers to the Γ point, this is no fundamental contradiction. Since O $2p$ states extend along the Cartesian axis, one should expect a strong spatial overlap between the O $2p_z$ and the Ti d_{z^2} and between the O $2p_{x,y}$ and the Ti $d_{x^2-y^2}$, giving rise to hybridizations.

B. Theory

The state-of-the art theoretical framework to describe absorption spectra from first principles is many-body perturbation theory (MBPT). In particular, in a solid one usually

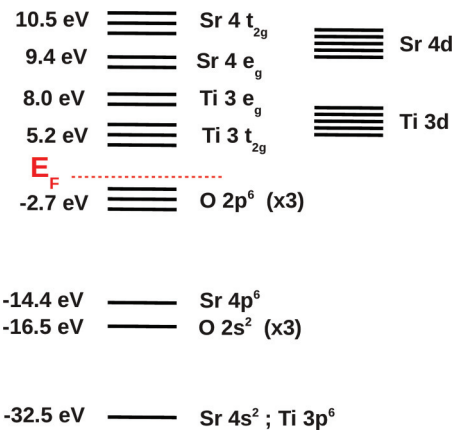

FIG. 2. (Color online) Calculated energy of electronic states in STO compared to Sr 4d and Ti 3d atomic levels. The ordering of the energy levels refers to the Γ point; the corresponding energies are average values taken from the l-DOS (see text).

works in a quasiparticle picture: the repulsive long-range Coulomb interaction between electrons leads to screening, i.e., electrons are surrounded by a positively charged cloud. These screened particles are called quasiparticles. Their Coulomb interaction is reduced, which justifies treating it as a perturbation. The quasiparticles are solutions of a Schrödinger-like equation, where the many-body exchange and correlation effects (corresponding to the difference between the bare particles and the quasiparticles) are described by a nonlocal, non-Hermitian, and energy-dependent operator called self-energy Σ.

The key ingredient is the one-particle (or two-point) Green's function $G_{\sigma,\sigma'}(\mathbf{r},t,\mathbf{r}',t')$, which describes the probability amplitude for the propagation of an electron (hole) from space and spin coordinates $(\mathbf{r}',\sigma')$ at time t' to $(\mathbf{r},\sigma)$ at time t (vice versa for the hole). In general, a good approximation for the self-energy is $\Sigma = iGW$ (for this reason, it is called the GW approximation),[30] where G stands for the one-particle Green's function and W denotes the screened Coulomb interaction. The GW approximation has shown its validity in many applications to metals, semiconductors, and insulators, in particular concerning the calculation of band gaps for the latter two.[37,38]

Often, the result of a GW correction with respect to the Kohn-Sham band structure, for example calculated in the LDA, is an essentially rigid shift of conduction bands with respect to valence bands. One can then simulate this result by a single number, the gap opening. In this case, the self-energy is mimicked by the so-called "scissor operator" (SO).

In the case of electron-hole excitations, as measured, for example, in optical absorption, one has to deal with two particles (the electron and the hole) evolving in the material, and eventually interacting, giving rise to an exciton. The equation taking into account these two-particle (or four-point) quantities is the so-called Bethe-Salpeter equation (BSE).[29,31]

This equation links the four-point correlation function L^0, which describes the two particles evolving without interacting with each other, to the (interacting) two-particle correlation function L:

$$L(1234) = L^0(1234) + L^0(1256)\Xi(5678)L(7834), \quad (1)$$

where n stands for $(\mathbf{r}_n,\sigma_n,t_n)$ and repeated variables are integrated over. The kernel of the BSE is $\Xi = \frac{\delta\Sigma}{\delta G}$. The standard approach to approximate Ξ is to assume the GW approximation for the self-energy and to neglect the derivative of W with respect to G. One gets hence $\Xi(5678) \approx i\delta(58)\delta(67)W(56)$. Moreover, most often the static limit of W is used.

In reciprocal space, the central quantity is then $W_{\mathbf{GG}'}(\mathbf{q},\omega)|_{\omega=0}$, where $W_{\mathbf{GG}'}(\mathbf{q},\omega) = \epsilon^{-1}_{\mathbf{GG}'}(\mathbf{q},\omega)v_{\mathbf{G}'}(\mathbf{q})$, with ϵ the dielectric function and v the bare Coulomb interaction. Contrary to v, the screened interaction W is not diagonal in the reciprocal-lattice vectors $\mathbf{GG}'$ because the screening takes the response of the inhomogeneities of the material into account. In solids, this effect can often be neglected in BSE calculations; therefore, W is usually taken to be diagonal in the $\mathbf{GG}'$ space.[39] We will come back to this point later. Another point to recall is the fact that L contains the density-density response to an external potential as measured, e.g., in electron-energy-loss spectroscopy, whereas here we are interested in absorption, where the response to the total classical potential is needed.

One has therefore to work with a slightly modified version of the BSE that consists in omitting the long-range part of the bare Coulomb kernel $v_{\mathbf{G}=\mathbf{0}}$; we call the remaining Coulomb kernel $\bar{v}$.[31]

The two-particle nature of the BSE allows one to solve the problem on a basis set represented by pairs of single-particle states. For electron-hole excitations, one can restrict the basis to pairs of occupied and empty orbitals (transitions). In this basis and with the static approximation to W, the BSE transforms to a standard two-particle Schrödinger equation with the excitonic Hamiltonian H^{exc} composed of the unperturbed transition energies on the diagonal, and matrix elements of Ξ. The coupling between transitions of positive and negative energies is most often neglected (Tamm-Dancoff approximation). The eigenvalues E_λ and eigenvectors $\mathbf{A}_\lambda$ of H^{exc} are then used to compute the macroscopic dielectric tensor ϵ_M in a form that is similar to the single-particle spectrum, but with modified transition energies E_λ and mixing of transitions due to the coefficients A_λ:

$$\epsilon_M(\omega) = 1 - \lim_{\mathbf{q}\to 0} v(\mathbf{q}) \sum_\lambda \frac{\left|\sum_T \tilde{\rho}_T(\mathbf{q})\mathbf{A}_\lambda^T\right|^2}{E_\lambda - \omega - i\eta}, \tag{2}$$

where T is the index of the independent-quasiparticle (IP) transition, $\tilde{\rho}_T$ is the corresponding dipole moment, and $i\eta$ is an imaginary infinitesimal quantity.

For a single excitonic peak at energy E_λ, the spectral weight is determined by the sum over IP transitions, $\sum_T \tilde{\rho}_T(\mathbf{q})\mathbf{A}_\lambda^T$. This mixing effect is important, because both the matrix elements and the coefficients carry a phase, which leads to interference. Considerable redistribution of oscillator strength can therefore be observed, although the transition energies are most often essentially unchanged, except for the case of bound excitons. Indeed, to first order in W the transition energy change in a solid is zero, so that interference effects dominate the observed excitonic effects. It is therefore most important to analyze this mixing when one wants to *understand*, and not merely describe, an absorption spectrum. This justifies the use of a scheme as the one which we have adopted here for the purpose of analysis, which gives direct access to the A_λ, instead of computationally more advantageous alternatives such as iterative inversions of the BSE, which we use to calculate spectra over a wide energy range.

Another in principle computationally more efficient alternative to the diagonalization of the BSE is to change the framework and work with time-dependent density-functional theory[32] (TDDFT). In that case, the many-body problem is transformed into a fictitious single-particle problem of independent Kohn-Sham particles in an effective density-dependent local potential. When the system undergoes an excitation, the resulting polarization corresponds to a density change, which leads to an induced potential. The response function can be expressed either as the response to the external perturbation V_{ext} or to the sum of external and induced potentials, the total potential V_{tot}. In the first case, the response function is the susceptibility. It contains the induced potential resulting from the induced density. In the second case, the induced potential is included in the total potential and the response function is the independent-particle polarizability χ^0, which is simply the sum of independent-particle transitions:

$$\chi^0_{\mathbf{G}\mathbf{G}'}(\mathbf{q},\omega) = \sum_{ij\mathbf{k}} \frac{\tilde{\rho}_{ij\mathbf{G}}(\mathbf{q})\tilde{\rho}^*_{ij\mathbf{G}'}(\mathbf{q})}{\omega - [\varepsilon_i(\mathbf{q}) - \varepsilon_j(\mathbf{k}+\mathbf{q})] + i\eta}, \tag{3}$$

where ε_i is the energy of the ith level and $\tilde{\rho}_{ij\mathbf{G}}(\mathbf{q}) = \langle\phi_{i\mathbf{k}}|e^{-i(\mathbf{q}+\mathbf{G})}|\phi_{j\mathbf{k}+\mathbf{q}}\rangle$. The single-particle energies ε_i and single-particle wave functions $\phi_i(\mathbf{r})$ are Kohn-Sham eigenvalues and eigenfunctions. In solids they are most often computed using simple functionals like the local density approximation (LDA)[40,41] for the exchange-correlation potential V_{xc}.

The susceptibility is then obtained by solving the Dyson equation:

$$\chi = \chi^0 + \chi^0(v + f_{\text{xc}})\chi, \tag{4}$$

where the Coulomb interaction v is the derivative of the Hartree potential with respect to the density, and the exchange and correlation kernel f_{xc} is the derivative of V_{xc}. The total kernel expresses the presence of the induced potentials. f_{xc} is unknown and must be approximated. In this work, we use three approximations for f_{xc}:

(i) The random-phase approximation (RPA), for which $f_{\text{xc}} = 0$.

(ii) The long-range contribution kernel (LRC), for which $f_{\text{xc}}(\mathbf{q},\omega) = -\alpha/\mathbf{q}^2$, with α determined by the RPA dielectric constant.[42,43]

(iii) The bootstrap kernel,[44] where α is determined through a self-consistent procedure.

To be precise, the latter two kernels are meant to simulate only a part of f_{xc}, namely the one corresponding to excitonic effects. Therefore, the GW correction must be added explicitly; this is done by using GW energies instead of Kohn-Sham ones in χ_0 (3). The same correction applied to the RPA is called RPA + GW.

From the susceptibility, the inverse microscopic dielectric matrix $\epsilon^{-1} = 1 + v\chi$ is obtained, and hence the macroscopic frequency-dependent dielectric function $\epsilon_M(\omega)$,

$$\epsilon_M(\omega) = \lim_{\mathbf{q}\to\mathbf{0}} \frac{1}{\epsilon^{-1}_{\mathbf{G}=\mathbf{0}\,\mathbf{G}'=\mathbf{0}}(\mathbf{q},\omega)}. \tag{5}$$

In the inversion of the matrix ϵ, the off-diagonal elements mix the independent-particle transitions. This is exactly the same mixing as the one induced by the bare Coulomb kernel $\bar{v}$ in the BSE. It accounts for the microscopic response of the system and corresponds to the crystal local field effects (LFEs). When neglecting the microscopic components of the response, one obtains the spectra without the local field effect (NLF). The result is merely Fermi's golden rule in the IP picture, corresponding to all A_λ^T being δ functions in Eq. (2). All theoretical spectra of STO that we found in the literature[11,14,15,18–24] are computed within the RPA + NLF approximation.

C. Computational details

Ground-state properties and GW corrections to Kohn-Sham eigenvalues have been computed with ABINIT,[45] a plane-wave-based software. Semicore pseudopotentials have been used in all calculations, including 40 electrons per cell. The Ti atom participates with 12 electrons [$3s^2 + 3p^6 + 4s^2 + 3d^2$], the Sr

atom with 10 $[4s^2 + 4p^6 + 5s^2]$, and each O atom participates with six electrons $[2s^2 + 2p^4]$. Working with semicore pseudopotentials is crucial because dividing an atomic shell into a core and a valence can lead to severe errors in the evaluation of the exchange term.[46] The pseudopotentials have been created partially in a doubly ionized configuration (for Sr and Ti). Core radii, within which the atomic pseudo-wave-functions are exact, were $r_c = 1.7$ Bohr for all components of Sr, 1.25 Bohr for Ti s and Ti p while $r_c = 1.65$ Bohr for the Ti d channel, and finally $r_c = 1.5$ Bohr for oxygen.

For the ground state, we performed LDA-DFT calculations (band structure and density of states) applying a cutoff of 70 Ha to the plane-wave basis set. The density of states has been calculated using a grid of 512 k points centered in Γ (35 k points in the irreducible wedge).

GW corrections have been evaluated with the G_0W_0 method,[47] with a cutoff energy of 32 Ha for the basis set and 25 Ha for the exchange and correlation components of the self-energy. A total of 80 bands have been included in the calculation of the self-energy, and 200 bands for the screening. For both screening and self-energy calculations, the same k-points grid as for the ground state has been used. The dimension of the screening matrix is of 2373×2373 **G** vectors (~ 25 Ha). To speed up the calculations, the Godby-Needs[48] plasmon pole approximation has been used. We have tested its validity by performing also calculations using contour deformation not reported in this paper. When applied, the SO shift is based on the results of these calculations, not on experimental results.

TDDFT spectra (RPA, LRC, and bootstrap) have been computed up to 15 eV using the DP code.[49] In the calculation of $\chi^0_{\mathbf{GG'}}$ we have summed over 31 bands to converge the spectrum in this energy range. The dimension of the matrix was 33×33, 1237 plane waves have been included in the basis set, and the irreducible Brillouin zone has been sampled with a grid of 512 shifted k points. In all TDDFT calculations, G_0W_0 energies have been used instead of LDA energies, except where explicitly specified.

The BSE has been solved using the EXC code.[50] Except for the spectra of Fig. 10, where the full diagonalization of the excitonic Hamiltonian has been performed, we used the Haydock diagonalization algorithm, with 150 iterations to achieve converged spectra. The number of plane waves, the range of energy, the dimension of the matrix, and the k-points grid used are the same as for the TDDFT calculations, except where explicitly specified.

III. RESULTS

This section is divided into two subsections. Section III A is devoted to the discussion of the band structure of the material. The analysis of on-site and angular momentum projected density of states (l-DOS) will allow us to discuss the character of the first 11 conduction bands. Section III B concerns the optical spectra. We solved the BSE up to 15 eV and we have compared our results with experimental data[14,33] as well as with our TDDFT calculations performed with three different kernels. The different role played by Ti $3d$ electrons and Sr $4d$ electrons is analyzed with reference to the l-DOS and the band structure discussed in the preceding section. We will support our discussion with arguments based on the crystal-field splitting and geometry considerations.

A. l-DOS and band structure

1. Distribution of quasiparticle corrections

The results of our LDA band-structure calculations (not reported in this paper) are in good agreement with experiments[11,12,14] and previous calculations.[11,14,18–22,24] LDA predicts a direct gap at Γ of 2.21 eV, much smaller than the experimental value of 3.75 eV.[14] This underestimation is the well-known Kohn-Sham band-gap problem. To correct the LDA band gap, we computed quasiparticle corrections within the perturbative G_0W_0 approximation. The resulting band structure is reported in Fig. 3.

As is the case in many materials, near the Fermi energy, GW corrections open the photoemission gap, giving a GW gap at Γ of 3.76 eV in very good agreement with the experimental value of 3.75 eV. To access the effect of GW corrections beyond the gap, quasiparticle corrections versus band index are reported in Fig. 4. For each band index i, the corrections are evaluated for the different k points in the Brillouin zone: the resulting line of dots accounts for the deformation of the corresponding band. G_0W_0 corrections mainly shift the bands, with a relative shift of 1.6 eV. One can notice that for the highest occupied molecular orbital (HOMO) (band 20) and the first three conduction bands (band indexes 21, 22, and 23), a rigid shift constitutes an excellent approximation.

Modifications of the band shape become more important for the three deepest bands (12, 13, and 14) as well as for conduction bands starting from index 24. These bands give rise to transitions around 7 eV, which correspond to energies where the electron-energy-loss spectrum displays its first structures.[14] In such a case, the validity of the plasmon pole model (PPM) has to be checked.[51] Using a contour deformation integration, we have verified that the dispersion of

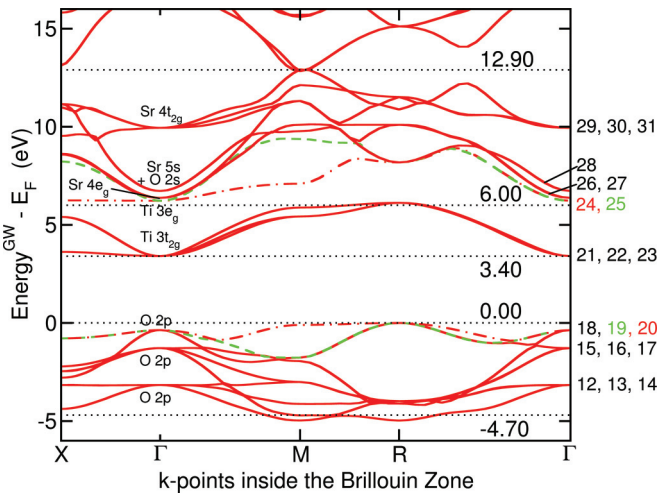

FIG. 3. (Color online) GW band structure along high-symmetry directions. We report the index of the band (right y axis) and its attribution (inside the plot) to specific atomic levels at the Γ point. Dotted lines are drawn according to notable structures in the l-DOS (Fig. 5). Peculiar bands have been highlighted with green dashed and red dashed-dotted lines.

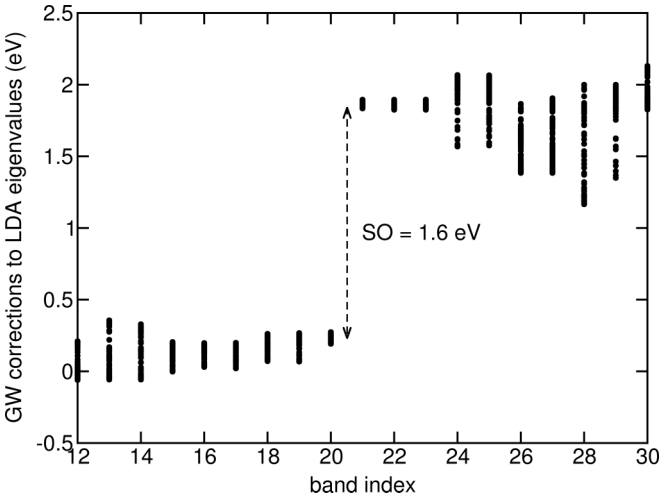

FIG. 4. Dispersion of G_0W_0 corrections along the bands.

our GW corrections was not due to the PPM. In any case, the deformation does not exceed 1 eV, and the separation in energy between the bands is large enough to be able to distinguish the projected states, thus the character of bands deduced from the LDA calculation will still be valid.

2. State assignment

The quite small deformation of the bands due to G_0W_0 corrections justifies using alternatively LDA eigenvalues corrected with G_0W_0 calculation or with a scissor operator (SO) of 1.6 eV. On the l-DOS reported in Fig. 5, we applied the scissor operator, while for the band plot of Fig. 3 we corrected LDA energies with a G_0W_0 calculation. In both cases the Fermi energy corresponds to 0 eV.

To calculate the on-site and angular momenta-projected l-DOS, we adjusted the radii of the spheres where wave functions were projected so that the sum of partial DOS matches the total DOS. The resulting radii are equal to 3.7 Bohr for Sr, 2.3 Bohr for Ti, and 2.2 Bohr for O. Figure 5 shows the total quasiparticle density of states and dominant on site-projected l-DOS for selected elements and angular momenta for energies ranging from −6 to 16 eV.

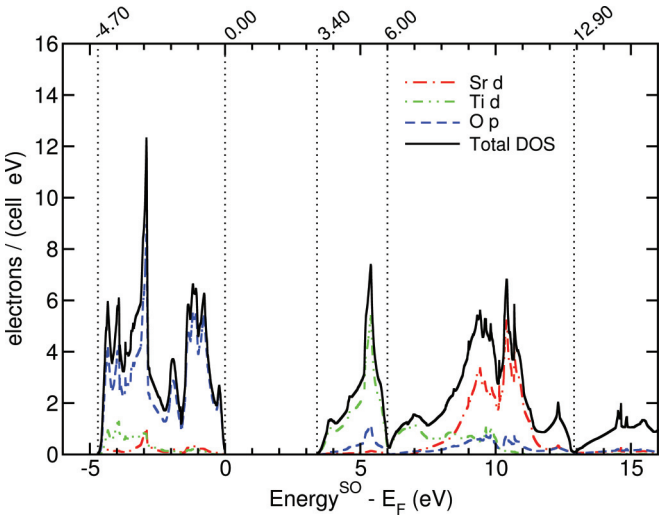

FIG. 5. (Color online) Total quasiparticle DOS and atom-centered L-projected DOS for the O $2p$, Ti $3d$, and Sr $4d$ states. Well-defined structures are separated by dotted vertical lines with a label for corresponding energy. Quasiparticle energies have been obtained shifting LDA eigenvalues by 1.6 eV (see Sec. III A1).

Three main structures can be identified: a part of the valence band extending from −4.7 eV to the Fermi energy, a first peaked structure in the conduction band extending from 3.4 to 6 eV, and a second broader group of structures between 6 and 12.9 eV. The high electronegativity of oxygen atoms drains almost all the $4s^2$ and $3d^2$ electrons from the Ti atom and the $5s^2$ electrons from the Sr atom, filling almost completely the O $2p$ levels: the valence band is essentially composed by O $2p$ states, which weakly hybridize with the Ti $3e_g$ levels, as expected from the strong spatial overlap between these states. The Fermi energy lays between the O $2p$ levels and the Ti $3d$ bands.

The first group of empty states has a predominant Ti $3d$ character: due to crystal-field symmetry, one can conclude that they are Ti $3t_{2g}$ levels that form an almost separate band (3.4–6 eV). The second group of structures (6–12.9 eV) has a predominant d-momentum character shared between the remaining Ti $3e_g$ levels and the whole Sr $4d$ subshell, expected to be also split in e_g and t_{2g} levels.

These assignments allow us to describe more precisely the band structure (Fig. 3) where GW energies for valence and conduction bands in the same energy range as Fig. 5 are plotted. We also draw horizontal dotted lines in correspondence with the vertical lines in the l-DOS plot. In the band plot, we recover the three main groups identified in the l-DOS: the valence band extending from around −4.7 eV to the Fermi level and formed by nine bands labeled from 12 to 20 corresponding to O $2p$. At higher energies we find a first group of three conduction bands (labeled 21, 22, and 23) extending between 3.4 and 6 eV due to Ti $3t_{2g}$ and finally a wider group of bands from 6 to 12.9 eV composed of eight bands (24 to 31).

The bands 24 and 25 can be assigned to e_g states of Ti with the support of the l-DOS. To identify the character of Sr states, we can use the crystal-field symmetry argument as well as the degeneracy of the bands at Γ: the bands 26 and 27 are assigned to the Sr $4e_g$ and the bands 29, 30, and 31 are assigned to Sr $4t_{2g}$.

A careful analysis of the l-DOS in this energy range shows the presence of Sr $5s$ hybridized with O $2s$ states (not shown for clarity). For this reason, we assigned the band 28 to Sr $5s$ states and O $2s$ in agreement with Ref. 36.

Concerning the dispersion of the bands, one can note the presence of regions where some bands are flat, especially along the ΓX direction, indicating localized states. Of particular interest for our following analysis are the two topmost valence bands (labeled 19 and 20) and the lower-energy Ti $3e_g$ level (band 24). One can notice that band 24 is flat along ΓX but strongly disperses in other parts of the BZ: the degree of localization changes along the same band.

B. Optical spectra

Let us now move to optical spectra. In Fig. 6, we report two BSE absorption spectra, computed, respectively, using GW corrections (black solid line) and the SO of 1.6 eV (red dashed

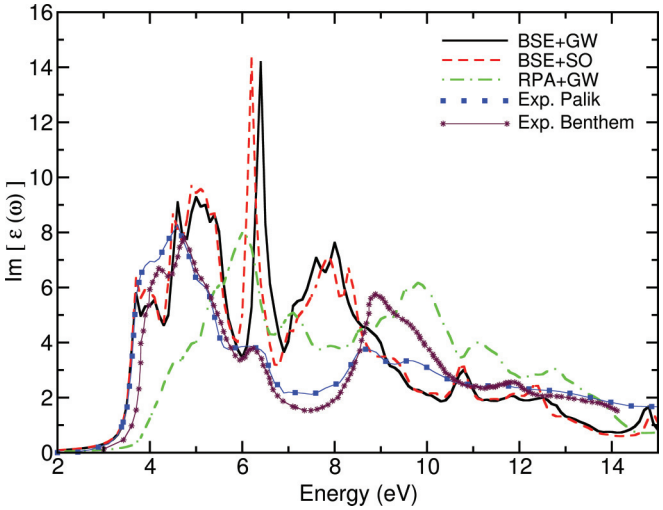

FIG. 6. (Color online) Absorption spectrum of STO: BSE + GW (black solid) and BSE + SO (red dashed), RPA + GW (green dashed-dotted), and experimental data from Palik[33] (blue dotted) and from Benthem[14] (violet crosses).

line) and compared with an RPA + GW (green dashed dotted line) and experimental data[14,33] (blue and violet dotted lines). Both calculations have been performed in the Tamm-Dancoff approximation. We checked that this approximation is indeed valid within the energy range of interest.

In the experimental spectrum we can identify three notable structures: a principal wide structure between 3.5 and 5.6 eV, a steplike bump between 5.6 and 7 eV, and finally a third wider group of peaks between 8 and 11 eV. The RPA spectrum without local fields is in good agreement with previous calculations.[21] Its agreement with experiment has the quality one can expect from an RPA calculation: the three structures identified in the experimental spectrum are present, with satisfying amplitudes. However, the position of the different structures is shifted to higher energy due to the lack of electron-hole interaction.

To include electron-hole interactions in the optical spectrum, we solved the BSE [Eqs. (1) and (2)]. Indeed, when the electron-hole interaction is taken into account through the resolution of the BSE, all the structures are moved to lower energies indicating a strong excitonic effect. Comparing the two BSE spectra, one notices that they are very similar. In both spectra, one can identify four structures of interest: a first group extending from the onset until about 6 eV, a strong and narrow peak around 6.3 eV, a group extending between 7 and 9.5 eV, and finally an isolated peak centered at 10.8 eV. The slight differences between the two BSE spectra arise from the distortion of the bands shown in Fig. 4 as compared to a simple rigid shift. The lowest energy feature comes from transitions between bands close to Fermi energy, where SO is a very good approximation: the two BSE spectra almost coincide. Farther from the absorption edge, GW corrections slightly modify the band dispersion with the consequence of a blueshift of 0.1 eV of the strong narrow peak at 6.3 eV, and minor modifications in the other structures. In the following, we will use GW, but our results indicate that SO may be used safely in more complex structures.

The comparison between RPA + GW and BSE + GW shows that the excitonic interaction reduces the optical gap leading to a shift of $\sim$ 0.8 eV of the peak at the onset. This is mainly an effect of the change in line shape; the corresponding exciton binding energy is only 0.22 eV.

The first BSE structure is on top of the experimental curve up to almost 4 eV, giving a very good description of the absorption onset. From 4 to 6 eV, the BSE spectrum loses some accuracy in the height of the peaks, but the position of the structure is well reproduced. This proves that excitonic effects are very important and should not be neglected to understand the optical spectrum of $SrTiO_3$.

The second structure predicted by the BSE calculation is a sharp peak centered at 6.4 eV. It is in the range of the steplike structure in experiment extending from 5.5 and 7 eV, but the calculated intensity is strongly overestimated. Concerning the third structure, the amplitude is too strong and the energy position is centered at 8 eV for the BSE calculation while it is 9 eV for the measured spectrum. These two facts indicate a too strong excitonic effect.

1. Independent-particle O 2p → Ti 3d and O 2p → Sr 4d transitions

In all calculations, the valence bands from 12 to 20 (O 2p) have been included. We have checked that inclusion of conduction bands up to 31 was sufficient to converge the spectrum up to 15 eV. To identify the role of different bands in the spectra, we reduced progressively the number of conduction bands included in the calculation.

We first analyze the RPA + GW spectra. We have checked (not presented in the paper) that the local field effects are negligible in the energy range considered here.[52] Thus the spectra reported in Fig. 7 are calculated without local field effects, i.e., without mixing the IP transitions, so that peaks can be directly related to the band structure.

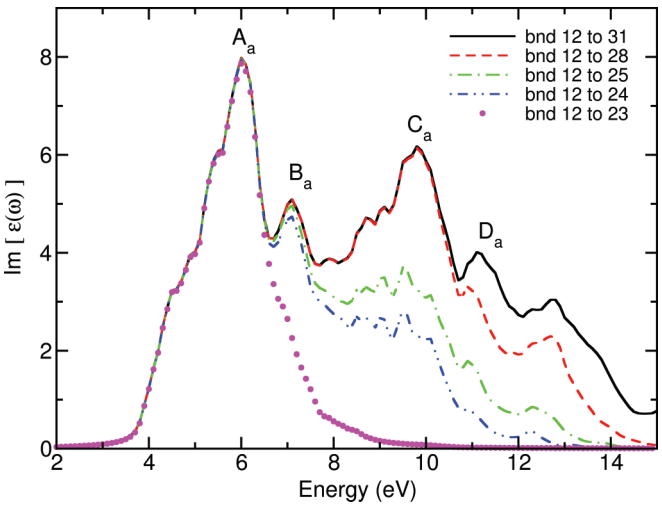

FIG. 7. (Color online) RPA + GW spectrum without local fields. Conduction bands included in the calculation are progressively reduced: up to band 31 (converged spectrum) (black solid), up to 28 (red dashed), up to 25 (green dashed-dotted), up to 24 (blue dashed-double dotted), and up to 23 (magenta plain circles).

Structure A_a is due to transitions from the valence to bands 21, 22, and 23, which have been assigned to Ti $3t_{2g}$ states. Since inclusion of higher conduction bands does not affect the A_a structure, we will infer that it is created by transitions involving *only* the Ti $3t_{2g}$ states.

Structure B_a is peaked at 7.1 eV. It is created by transitions to band 24 which alone account for more than 80% of the spectral weight, and it attains full convergence including band 25. It is completely ascribed to transitions to the two Ti $3e_g$ states.

We note that the two Ti $3e_g$ states contribute also to the formation of all the other spectral features, as expected from their density of states ranging to 11 eV; in particular, C_a is for around 50% due to these states, the remaining part coming from transitions to bands 26, 27 (Sr $4e_g$), and band 28 that we have assigned to a hybridized Sr $5s$–O $2s$ state. The inclusion of bands 29, 30, and 31 (Sr $4t_{2g}$) allows the full convergence of the spectrum.

Since peak B_a is of particular interest for the sharp excitonic peak, we investigated in greater detail the origin of the transitions in the Brillouin zone. In Fig. 8, we show RPA + GW spectra calculated including all Ti $3d$ states—conduction bands 21 to 25 (red solid line) and calculated excluding Ti $3d$, but including Sr $3d$ states—conduction bands 26 to 31 (blue dashed-double dotted line). The full spectrum (black plain circles) is the sum of these two contributions. These three spectra are computed by summing transitions over all the 512 k points sampling the Brillouin zone. The green dashed-dotted line corresponds to a spectrum calculated including all Ti $3d$ states—conduction bands 21 to 25—but we suppressed in the summation the transitions from valence bands 19 and 20 to conduction band 24 and arising from k points that fall into three cylinders enclosing the ΓX axes of the BZ: the B_a peak disappears. This demonstrates that this peak is mainly due to transitions from bands 19 and 20 (top valence O $2p$) to conduction bands 24 (Ti $3e_g$), and at k points along ΓX. As already mentioned in Sec. II A, these bands are flat, corresponding to well-localized states.

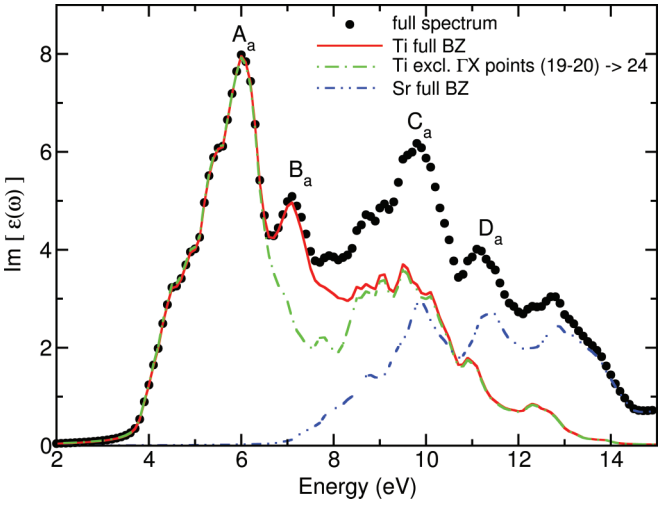

FIG. 8. (Color online) RPA + GW spectra without local fields: full spectrum (black plain circles); spectrum up to band 25 (thus including all Ti $3d$ states) (red continuous line); the same spectrum calculated excluding transitions from bands 19 and 20 to band 24 around the ΓX path of the Brillouin zone (green dashed-dotted); spectrum including *only* conduction bands from 26 to 31, corresponding to Sr $4d$ states and the band 28 (blue double-dot dashed).

Peak C_a is due for about 50% to transitions to bands 24 and 25. We checked that the valence bands involved are the bands 12 to 17. The remaining part involves transitions from all valence states to bands 26, 27, and 28.

2. *Electron-hole interaction in O 2p → Ti 3d and O 2p → Sr 4d*

The same analysis as in the previous subsection has been adopted for the BSE + GW calculation of the spectrum (see Fig. 9). Parent structures have been labeled with the same letters (A, B, C, and D).

As in the RPA case, one can see that the group A_b is completely described by the inclusion of the bands 21, 22, and 23, corresponding to O $2p \rightarrow$ Ti $3t_{2g}$ transitions. The inclusion of bands 24 and 25 is once again responsible for the creation of the structure labeled B_b at 6.4 eV (with a shift in energy of ∼0.8 eV with respect to B_a). In the RPA case, band 24 was responsible for around 80% of the peak, and band 25 for the remaining. In the excitonic case, each band accounts for more or less half of the amplitude. This peak is very sharp and narrow.

As for the RPA calculation, bands 24 and 25 create half of the C_b peak centered at around 8 eV, the remaining part coming from the Sr $4e_g$ states (bands 26 to 28). The energy difference between C_b and C_a is ∼2 eV, corresponding to a very large excitonic effect.

The structure D_b, located at 10.8 eV, is formed essentially by Sr $4t_{2g}$ states as it is determined only by bands 29, 30, and 31. The excitonic effect on D_b is much smaller.

This analysis shows that the bands 24 and 25 play a major and intriguing role in the formation of the two excitonic structures B_b and C_b. Transitions arising from these bands on the one hand give the strong and narrow exciton B_b, and on the other hand contribute to the much broader exciton C_b. We have seen that band 24 has a character that depends on its momentum **k**. Along the ΓX direction it is flat, and in the other parts of the BZ it is dispersing. Since we expect the strong

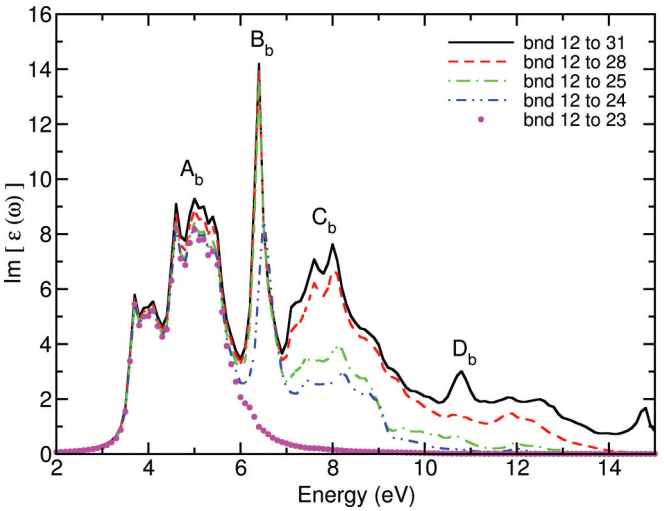

FIG. 9. (Color online) BSE + GW spectrum. Conduction bands included in the calculation are progressively reduced. The color and line code is the same as in Fig. 7

and narrow exciton B_b to arise from localized (nondispersing) states, we suggest that B_b is essentially created by transitions from valence bands 19 and 20 to the conduction band 24 along the ΓX direction. Transitions to 24 and 25 giving rise to the C_b broad excitonic peak (and the background that contributes to the total amplitude of B_b) come from the much more dispersing 12 to 18 valence bands, as well as from 19 and 20 to 24 excluding the ΓX direction. The remaining part of the broad C_b exciton is due to transitions to Sr $4e_g$.

3. Mixing of O → Ti transitions: Interference effects

Since the excitonic effects mix the single-particle transitions, we analyze the spectral weights $\tilde{\rho}_T A^T_\lambda$ entering in Eq. (2) and leading to the optical spectrum. The coefficients $\mathbf{A}^T_\lambda$ give the weight and phase with which the various independent-particle transitions T contribute. Let us first concentrate on the weight. This is readily analyzed by plotting $|\mathbf{A}^T_\lambda|^2$ as a function of the GW transition energies E_T for a given excitonic energy E_λ. The space of transitions is in principle continuous; therefore, the result is given as a histogram where each segment contains transitions in a range of 100 meV. Figure 10 shows the result for the peak B_b, where $E_\lambda = 6.4$ eV. Without mixing transitions, one would find a δ peak. Because of the mixing, there is instead a broad distribution with a pronounced asymmetry, extending more toward higher than lower energies. To situate the energy range, the figure also shows the BSE and RPA spectra.

From the histogram alone, it is difficult to get a quantitative idea of the role of higher-energy transitions: toward that end, one has to consider also the phase of the various contributions. One way to do this is to introduce the partial spectral weight[53]

$$S_{E_\lambda}(E) = \left| \sum_{T:E_T \leqslant E} \tilde{\rho}_T \mathbf{A}^T_\lambda \right|^2, \tag{6}$$

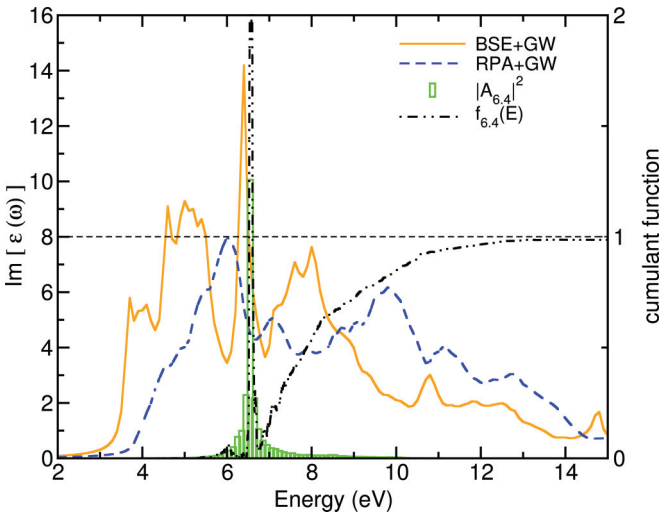

FIG. 10. (Color online) The weight of each transition T is expressed by the excitonic wave-function coefficient $|A^T_{6.4}|$ here reported in arbitrary units (green boxes). The value of the cumulant function $f_{6.4}$(E) is shown by a black dashed-double dotted line with the scale on the right axis. BSE + GW (orange solid) and RPA + GW (blue dashed) without local fields are also reported.

i.e., the sum of all independent-particle transitions with energy E_T smaller than a given value E. Since the excitonic mixing is quite restricted in energy, $S_{E_\lambda}(E)$ converges toward a plateau value S_λ for increasing E, and one can work with the normalized cumulant function

$$f_{E_\lambda}(E) = \frac{S_\lambda(E)}{S_\lambda}. \tag{7}$$

This function[54] for the peak energy $E_\lambda = 6.4$ eV is given by the black dashed double-dotted curve in Fig. 10.

One distinguishes two transition energy ranges: the first region is composed of RPA transitions located between 5.5 and 6.8 eV. These are transitions involving the Ti $3t_{2g}$ states. The maximum of $|A^T_{6.4}|^2$ falls in this energy range. This, however, does not mean that these transitions dominate the final spectrum: because of the phase factors, $f_{6.4}(E)$ first indeed builds up to a sharp peak with increasing E, but this rise is followed by a steep decrease indicating a destructive interference, until the final result is almost zero around 6.8 eV. The important contribution to B_b is then given by the second energy range, extending from 6.8 eV to higher energies. It is composed of the independent GW transitions involving the Ti $3e_g$ levels. Here $f_{6.4}(E)$ exhibits a quite monotonic rise that tends to the plateau value of 1. The function reaches 0.5 around 7.5 eV, corresponding to the peak B_a in the RPA + GW spectrum. The remaining contribution essentially comes from transitions associated with peak C_a. These findings confirm our previous analysis based on Fig. 9.

4. Localized excitations and the screening of the electron-hole pair

The previous results have been obtained using the standard approximations to the Bethe-Salpeter equation. For bulk systems, this includes the fact that the matrix $W_{\mathbf{GG}'}$ is taken to be diagonal in the reciprocal-lattice vectors. This is exact only for homogeneous systems: the off-diagonal elements of W are due to the off-diagonal elements of the inverse dielectric matrix. These elements contain the information that the variation of an external potential V_{ext} on a certain length scale can induce variations of the total potential V_{tot} in the material on another length scale, since

$$\epsilon^{-1}_{\mathbf{GG}'}(\mathbf{q},\omega) = \frac{\partial V^{\text{tot}}_{\mathbf{G}}(\mathbf{q},\omega)}{\partial V^{\text{ext}}_{\mathbf{G}'}(\mathbf{q},\omega)}. \tag{8}$$

The effect can often be neglected in optical spectra of bulk materials, when the density is quite homogeneous or, on the contrary, for strongly localized (e.g., core) electrons that are not polarizable enough to give a sizable contribution to the induced potential. Moreover, the exciton may extend over an area that averages out the inhomogeneities of the material. However, in other systems such as clusters, one has to go beyond the diagonal approximation. In a material like STO, one has to be careful, since, as we have seen above, excitations of quite different character contribute to the spectrum. In particular, peak B_b is a candidate for a more careful study, since localized states play a role. Indeed, Fig. 11 compares the result of a standard BSE calculation using a diagonal W (same as previous figures) to the result obtained when the full matrix $W_{\mathbf{GG}'}$ is taken into account.

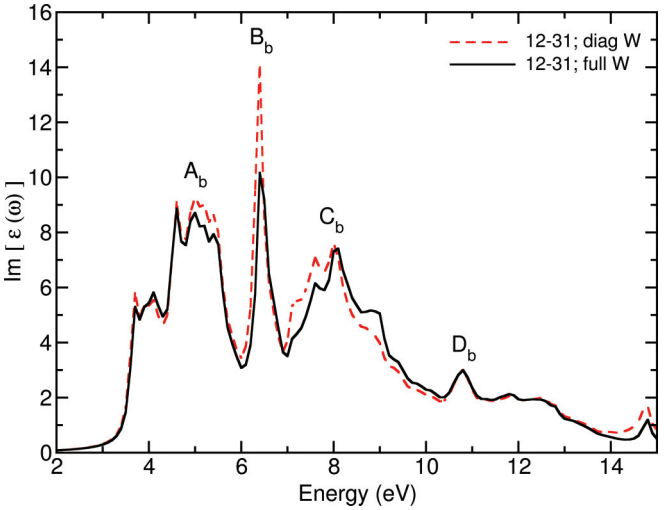

FIG. 11. (Color online) BSE + GW spectrum with diagonal and full-matrix screening $W_{GG'}$. Red dashed line: diagonal W for bands 12–31; black solid line: full W for bands 12–31.

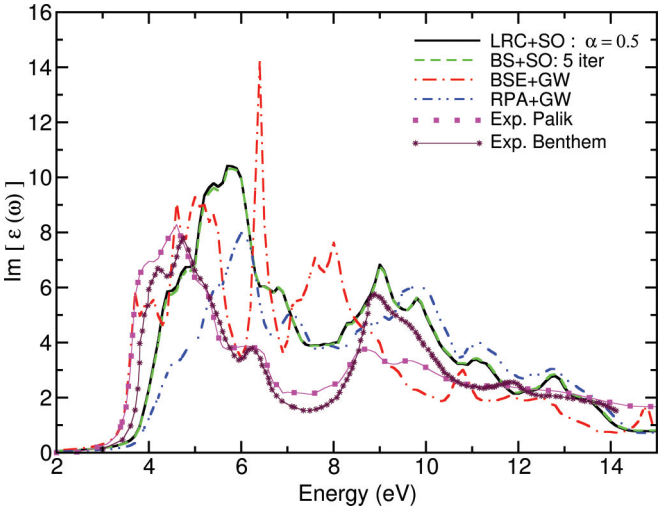

FIG. 12. (Color online) TDDFT calculations using LRC (black solid) and bootstrap (green dashed) kernels. They are almost superimposed. The experimental spectra are from Palik[33] (pink connected squares) and from Benthem[14] (violet crosses). The results of a BSE + GW calculation (red dash-dotted) and of an RPA + GW calculation (blue dashed-double-dotted) are shown for comparison.

The inclusion of the off-diagonal elements leads to minor changes concerning the C_b structure, A_b and D_b are totally unaffected. Instead, the excitonic peak B_b is reduced by almost a factor of 2. There is hence significant improvement concerning the agreement between theory and experiment, when the local polarizability of the electrons is correctly taken into account.

Nevertheless, the agreement is still not perfect, with the calculated B_b peak noticeably sharper than in experiment. We expect that this may be due to the neglect of other coupling terms in the approach used here: first, we have used the standard static screening approximation to the BSE, meaning that the one-particle Green's functions in L_0 are used in the quasiparticle approximation, and that the screening of the electron-hole interaction in W is taken at $\omega = 0$. Instead, one should in principle use the full one-particle Green's function including the quasiparticle damping and its satellite structure, as well as the frequency-dependent W. These two kinds of dynamical effects, which contain the coupling of the primary excitation to other neutral excitations of the system, are known to cancel each other to a large extent in simple semiconductors.[55] However, this may no longer be true in a more complex material with states of a different nature. The dominant effect of the dynamical contribution would be a damping of peaks. Second, we do not take into account electron-phonon coupling. The latter may be a source of errors in oxide perovskite, known to have a strong electron-phonon coupling constant and thus is prone to host polaronic[26–28] excitations that can modify strongly the absorption spectrum.

5. *Excitons via TDDFT*

BSE calculations are computationally heavy, even when the SO is used instead of state-dependent GW corrections. As outlined above, in principle also TDDFT gives access to optical spectra in a more efficient way. Especially for the description of continuum excitons, relatively simple kernels have been designed that allow one to perform calculations with an effort comparable to the RPA. It is therefore interesting to test various TDDFT flavors in the case of STO, where our BSE results can be considered as benchmarks, and where one would eventually like to carry out calculations for more complex structures, such as interfaces, for which BSE calculations might reach their limit of feasibility.

We have performed a series of tests with two TDDFT kernels designed to include excitonic effects: the LRC[42] and the more recent bootstrap kernel.[44] One should not expect very good agreement at the onset, where the BSE predicts a bound exciton, but it is still interesting to investigate whether deviations lie in a tolerable range. Moreover, one may think to obtain a good description in the range of the continuum excitons, where interference effects dominate. In the spirit of searching for a simple approach, we use the SO to simulate GW calculations, as we have shown above the quality of this approximation. The result of these calculations is reported in Fig. 12 where also BSE + GW, RPA + GW, and the experimental spectra are shown for comparison.

As can be expected in view of the similar structure of the LRC and the Bootstrap kernel, and in particular their behavior as $-c/\mathbf{q}^2$ for $\mathbf{q} \to \mathbf{0}$, the two approximations act in a similar way: the effect of both kernels is to transfer oscillator strength to lower energies with respect to the RPA + SO spectrum, such simulating the effect of the electron-hole interaction. In the case of LRC, the constant c that determines the $\mathbf{q} \to \mathbf{0}$ divergence of the kernel is a material-dependent scalar parameter α which is determined by an established linear relation[42] between α and the macroscopic dielectric constant ϵ_∞^{-1}. We have used the value $\epsilon_\infty = 6.4$ as calculated in RPA + LDA and found $\alpha = 0.5$. The results are not very sensitive to the precise value of α. In the case of the bootstrap kernel, the proportionality term is computed

self-consistently from ϵ_∞^{-1}. Five iteration cycles have been enough to converge the parameter c. This leads to a similar value of $c = 0.478$, and therefore it finally yields results that are almost undistinguishable from those of the LRC kernel. In both cases, as expected, the presence of a bound exciton at the onset cannot be well reproduced, and the spectrum therefore exhibits a blueshift of the order of 1 eV. Still, about 50% of the RPA + GW error is removed by the TDDFT calculations. Excitonic effects are weaker than in the BSE spectrum over the whole energy range. In particular, peak B_b remains a shoulder, though it is enhanced by the electron-hole interaction, and also the rest of the spectrum is less modified by the electron-hole interaction than through the BSE. This leads to a puzzling situation: apart from the onset region, the agreement between the approximate TDDFT results and experiment turns out to be better than when the BSE is used.

However, this should not induce us to think that the TDDFT is superior. These kernels have been derived from the BSE, and deviations have to be considered as errors. Improved results must therefore involve some error canceling. On the one hand, we have of course the simplified LRC-like form of the tested kernels. Moreover, in both cases one constant value was chosen for the proportionality constant c. However, it has been shown[56] that the constant approximation is valid only over a restricted energy range, whereas improved results over a wider range are obtained with a frequency-dependent prefactor. With the relation between parameters given by Botti and co-workers,[56] we find that c is increased by more than a factor of 2 around B_b, which leads to a slight redshift of the peaks (results not shown here). The discrepancy to the BSE is reduced, but only very partially, and B_b remains a shoulder instead of a sharp peak. In other words, the simple LRC form of the kernel, even when augmented with a frequency-dependent term, cannot capture the complexity of the BSE. It is, however, still interesting to note that the rough approximation to TDDFT leads to better agreement with experiment than the BSE in the high-energy range: though based on error canceling as stated above, this should not be considered as a pure coincidence. Rather, a reduced kernel can visibly simulate to some extent the reduction of the electron-hole interaction due to coupling effects that are neglected, e.g., damping due to dynamical effects. Further investigation in this direction might be worthwhile for future work.

IV. CONCLUSION

In conclusion, the optical spectrum of $SrTiO_3$ shows strong excitonic effects. Hence, an independent-particle description is not sufficient to obtain good agreement with experiment. There is a bound exciton and significant shift of oscillator strength at the onset that are well described by state-of-the-art Bethe-Salpeter calculations in the framework of the GW approximation. Transitions between localized electronic states dominate the spectrum between 6 and 7 eV, leading to a sharp excitonic peak. This peak is overestimated when the spatial resolution of the screening of the localized electron-hole pair is not taken into account. Going beyond this standard approximation to Bethe-Salpeter calculations in solids, the peak is reduced, but it still remains too sharp as compared to experiment, and a further structure around 8 eV also shows too strong excitonic effects.

We explain this discrepancy by the neglect of coupling to other excitations, which could be phonons and/or neutral electronic excitations contained in principle in the screening of the electron, hole, and electron-hole pair: with the QP approximation to the electron and hole, and the static approximation to the electron-hole interaction, these possible excitations are lost.

TDDFT in simple long-range approximations to the exchange-correlation kernel recovers about 50% of the RPA + GW error at the onset, and it yields a better description of the higher-energy part of the spectrum than the BSE, which should be due to error canceling. Overall, it turns out that one has to go beyond state-of-the-art Bethe-Salpeter calculations in order to obtain quantitatively correct description of the absorption spectrum of $SrTiO_3$. However, we have also shown that one can obtain agreement with experiment on a level that is sufficient to analyze the various structures and explain their origin by using computationally efficient approximate approaches, including the scissor operator to replace GW corrections to the band structure, and TDDFT using a simple long-range kernel.

ACKNOWLEDGMENTS

We acknowledge discussion with and help from M. Gatti, M. Guzzo, and J. Vidal. This work has been financed by the Chaire Energies Durables: a partnership between Ecole Polytechnique, the Fondation Européenne pour les Energies de Demain, and EDF. Computer time was granted by GENCI (project 544).

[1] M. S. Kim and C. H. Park, J. Kor. Phys. Soc. **1**, 490 (2010).
[2] C. E. Ekuma, M. Jarrell, J. Moreno, and D. Bagayoko, AIP Adv. **2**, 012189 (2012).
[3] M. Betzinger, C. Friedrich, A. Görling, and S. Blügel, Phys. Rev. B **85**, 245124 (2012).
[4] M. Jourdan, N. Blümer, and H. Adrian, Eur. Phys. J. B **33**, 25 (2003).
[5] A. Ohtomo and H. Y. Hwang, Nature (London) **427**, 423 (2004).
[6] J. G. Bednorz and K. A. Müller, Phys. Rev. Lett. **52**, 2289 (1984).
[7] F. Bottin and F. Finocchi, Phys. Rev. B **76**, 165427 (2007).
[8] R. Loetzsch, A. Lübcke, I. Uschmann, E. Förster, V. Große, M. Thuerk, T. Koettig, F. Schmidl, and P. Seidel, Appl. Phys. Lett. **96**, 071901 (2010).
[9] R. Evarestov, E. Blokhin, D. Gryaznov, E. A. Kotomin, R. Merkle, and J. Maier, Phys. Rev. B **85**, 174303 (2012).
[10] J. Inaba and T. Katsufuji, Phys. Rev. B **72**, 052408 (2005).
[11] M. Cardona, Phys. Rev. **140**, A651 (1965).
[12] D. Bäuerle, W. Braun, V. Saile, G. Sprüssel, and E. E. Koch, Z. Phys. B **29**, 179 (1978).
[13] J. L. Servoin, Y. Luspin, and F. Gervais, Phys. Rev. B **22**, 5501 (1980).
[14] K. van Benthem, C. Elsässer, and R. H. French, J. Appl. Phys. **90**, 6156 (2001).
[15] J. E. Jellison, Jr., L. A. Boatner, D. H. Lowndes, R. A. McKee, and M. Godbole, Appl. Opt. **33**, 6053 (1994).

[16]D. J. Lee, Y. K. Seo, Y. S. Lee, and H.-J. Noh, Solid State Commun. **150**, 301 (2012).
[17]A. H. Kahn and A. J. Leyendecker, Phys. Rev. **135**, A1321 (1964).
[18]L. F. Mattheiss, Phys. Rev. B **6**, 4718 (1972).
[19]R. Ahuja, O. Eriksson, and B. Johansson, J. Appl. Phys. **90**, 1845 (2001).
[20]Y. X. Wang, W. L. Zhong, C. L. Wang, and P. L. Zhang, Solid State Commun. **120**, 133 (2001).
[21]M. Arai, S. Kohiki, H. Yoshikawa, S. Fukushima, Y. Waseda, and M. Oku, Phys. Rev. B **65**, 085101 (2002).
[22]M.-Q. Cai, Z. Yin, and M.-S. Zhang, Chem. Phys. Lett. **388**, 223 (2004).
[23]G. Gupta, T. Nautiyal, and S. Auluck, Phys. Rev. B **69**, 052101 (2004).
[24]C. B. Samantaray, H. Sim, and H. Hwang, Microelec. J. **36**, 725 (2005).
[25]A. J. Nozik, Physica E **14**, 115 (2002).
[26]J. T. Devreese, S. N. Klimin, J. L. M. van Mechelen, and D. van der Marel, Phys. Rev. B **81**, 125119 (2010).
[27]W. S. Choi, H. Ohta, S. J. Moon, Y. S. Lee, and T. W. Noh, Phys. Rev. B **82**, 024301 (2010).
[28]C. Z. Bi, J. Y. Ma, J. Yan, X. Fang, B. R. Zhao, D. Z. Yao, and X. G. Qiu, J. Phys.: Condens. Matter **18**, 2553 (2006).
[29]A complete presentation of MBPT can be found in G. Strinati, Riv. Nuovo Cimento **11**, 1 (1988).
[30]L. Hedin, Phys. Rev. **139**, A796 (1965).
[31]For a general overview on TDDFT and MBPT refer, e.g., to G. Onida, L. Reining, and A. Rubio, Rev. Mod. Phys. **74**, 601 (2002).
[32]E. Runge and E. K. U. Gross, Phys. Rev. Lett. **52**, 997 (1984).
[33]*Handbook of Optical Constants of Solids II*, edited by E. D. Palik (Academic, San Diego, 1991).
[34]R. W. G. Wycoff, *Crystal Structures II* (Interscience, New York, 1964).
[35]R. G. Burns, *Mineralogical Applications of Crystal Field Theory*, 2nd ed. (Cambridge University Press, London, UK, 1993).
[36]L. van Heeringen, Master's thesis, Radboud University Nijmegen, 2012.
[37]W. G. Aulbur, L. Jönsson, and J. W. Wilkins, Solid State Phys. **54**, 1 (1999).
[38]F. Aryasetiawan and O. Gunnarsson, Rep. Prog. Phys. **61**, 237 (1998).
[39]S. Albrecht, L. Reining, R. Del Sole, and G. Onida, Phys. Rev. Lett. **80**, 4510 (1998).
[40]P. Hohenberg and W. Kohn, Phys. Rev. **136**, B864 (1964).
[41]W. Kohn and L. J. Sham, Phys. Rev. **140**, A1133 (1965).
[42]S. Botti, F. Sottile, N. Vast, V. Olevano, L. Reining, H.-C. Weissker, A. Rubio, G. Onida, R. Del Sole, and R. W. Godby, Phys. Rev. B **69**, 155112 (2004).
[43]L. Reining, V. Olevano, A. Rubio, and G. Onida, Phys. Rev. Lett. **88**, 066404 (2002).
[44]S. Sharma, J. K. Dewhurst, A. Sanna, and E. K. U. Gross, Phys. Rev. Lett. **107**, 186401 (2011).
[45]The ABINIT code is a common project of the Université Catholique de Louvain, Corning Incorporated, and other contributors; see http://www.abinit.org.
[46]Including semicore electrons is crucial in the computation of the GW corrections, as can be seen comparing our results of Kim and co-workers[1] and as demonstrated clearly in M. Rohlfing, P. Krüger, and J. Pollmann, Phys. Rev. Lett. **75**, 3489 (1995).
[47]Since the localized d states are empty, self-consistency is not crucial for this material.
[48]R. W. Godby and R. J. Needs, Phys. Rev. Lett. **62**, 1169 (1989).
[49]The DP code page is http://dp-code.org/.
[50]EXC is distributed at http://theory.polytechnique.fr/codes/exc/.
[51]A. Fleszar and W. Hanke, Phys. Rev. B **71**, 045207 (2005).
[52]At energies around 23 eV, neglecting the local fields gives rise to an absorbing structure that is completely washed out instead when local fields are accounted for. This feature is common to other transition-metal oxides structures such as $BaTiO_3$ and $CaTiO_3$.
[53]L. Yang, J. Deslippe, C. H. Park, M. L. Cohen, and S. G. Louie, Phys. Rev. Lett. **103**, 186802 (2009).
[54]Indeed at this energy the excitons are in the continuum, so infinitely many excitons can be found within a small interval in energy (we computed ≈1300 excitons between 6.2 and 6.4 eV). Moreover, in some case they can also be degenerate. The curve we show here is actually taken from one exciton only. This has been chosen because it clearly shows the common features of all the excitons in the range, that is, the interference peak and the monotonic convergence of the function f_λ. Choosing to analyze a different exciton in this range would not change our conclusions.
[55]F. Bechstedt, K. Tenelsen, B. Adolph, and R. Del Sole, Phys. Rev. Lett. **78**, 1528 (1997).
[56]S. Botti, A. Fourreau, F. Nguyen, Y.-O. Renault, F. Sottile, and L. Reining, Phys. Rev. B **72**, 125203 (2005).